EBioMedicine 42 (2019) 43–53

Contents lists available at ScienceDirect

EBioMedicine

journal homepage: www.ebiomedicine.com

EBioMedicine
Published by THE LANCET

New Noonan syndrome model mice with *RIT1* mutation exhibit cardiac hypertrophy and susceptibility to β-adrenergic stimulation-induced cardiac fibrosis

Shingo Takahara [a,b], Shin-ichi Inoue [a,*], Sachiko Miyagawa-Tomita [c,d,e], Katsuhisa Matsuura [f,g], Yasumi Nakashima [h], Tetsuya Niihori [a], Yoichi Matsubara [a,i], Yoshikatsu Saiki [b], Yoko Aoki [a,*]

[a] Department of Medical Genetics, Tohoku University Graduate School of Medicine, Sendai, Japan
[b] Division of Cardiovascular Surgery, Graduate School of Medicine, Tohoku University, Sendai, Japan
[c] Department of Pediatric Cardiology, Tokyo Women's Medical University, Tokyo, Japan
[d] Department of Physiological Chemistry and Metabolism, Graduate School of Medicine, The University of Tokyo, Tokyo, Japan
[e] Department of Animal Nursing Science, Yamazaki University of Animal Health Technology, Tokyo, Japan
[f] Institute of Advanced Biomedical Engineering and Science, Tokyo Women's Medical University, Tokyo, Japan
[g] Department of Cardiology, Tokyo Women's Medical University, Tokyo, Japan
[h] Department of Pediatrics, Seirei Hamamatsu General Hospital, Hamamatsu, Japan
[i] National Center for Child Health and Development, Tokyo, Japan

ARTICLE INFO

Article history:
Received 10 December 2018
Received in revised form 27 February 2019
Accepted 6 March 2019
Available online 18 March 2019

Keywords:
Noonan syndrome
RIT1
Cardiac hypertrophy
Cardiac fibrosis
AKT

ABSTRACT

Background: Noonan syndrome (NS) is a genetic disorder characterized by short stature, a distinctive facial appearance, and heart defects. We recently discovered a novel NS gene, *RIT1*, which is a member of the RAS subfamily of small GTPases. NS patients with *RIT1* mutations have a high incidence of hypertrophic cardiomyopathy and edematous phenotype, but the specific role of *RIT1* remains unclear.
Methods: To investigate how germline *RIT1* mutations cause NS, we generated knock-in mice that carried a NS-associated *Rit1* A57G mutation ($Rit1^{A57G/+}$). We investigated the phenotypes of $Rit1^{A57G/+}$ mice in fetal and adult stages as well as the effects of isoproterenol on cardiac function in $Rit1^{A57G/+}$ mice.
Findings: $Rit1^{A57G/+}$ embryos exhibited decreased viability, edema, subcutaneous hemorrhage and AKT activation. Surviving $Rit1^{A57G/+}$ mice had a short stature, craniofacial abnormalities and splenomegaly. Cardiac hypertrophy and cardiac fibrosis with increased expression of S100A4, vimentin and periostin were observed in $Rit1^{A57G/+}$ mice compared to $Rit1^{+/+}$ mice. Upon isoproterenol stimulation, cardiac fibrosis was drastically increased in $Rit1^{A57G/+}$ mice. Phosphorylated (at Thr308) AKT levels were also elevated in isoproterenol-treated $Rit1^{A57G/+}$ hearts.
Interpretation: The A57G mutation in *Rit1* causes cardiac hypertrophy, fibrosis and other NS-associated features. Biochemical analysis indicates that the AKT signaling pathway might be related to downstream signaling in the RIT1 A57G mutant at a developmental stage and under β-adrenergic stimulation in the heart.
Fund: The Grants-in-Aid were provided by the Practical Research Project for Rare/Intractable Diseases from the Japan Agency for Medical Research and Development, the Japan Society for the Promotion of Science KAKENHI Grant.

1. Introduction

The RAS/mitogen-activated protein kinase (MAPK) signaling pathway plays a crucial role in cell proliferation, differentiation, development and apoptosis [1–4]. Dysregulation of this pathway leads to carcinogenesis and developmental disorders. Germline mutations in components of the RAS/MAPK pathway cause autosomal dominant or recessive congenital anomaly syndromes, termed "RASopathies", which typically show distinctive facial features, short stature, intellectual disability and congenital heart defects [4–7]. The features of RASopathies usually result from hyperactivation of the RAS/MAPK pathway [4,6]. Noonan syndrome (NS) is a relatively common type of RASopathy [8,9]. Tartaglia and his colleagues first reported that

* Corresponding authors at: Department of Medical Genetics, Tohoku University School of Medicine, 1-1 Seiryo-machi, Aoba-ku, Sendai 980-8574, Japan.
E-mail addresses: sinoue@med.tohoku.ac.jp (S. Inoue), aokiy@med.tohoku.ac.jp (Y. Aoki).

https://doi.org/10.1016/j.ebiom.2019.03.014

Research in context

Evidence before this study

Noonan syndrome (NS) is a relatively common genetic disorder that is characterized by short stature, a distinctive facial appearance, and heart defects. We discovered a novel NS gene, *RIT1*, which is a member of the RAS oncogenes, in 2013. Genotype-phenotype analysis of NS patients with a *RIT1* mutation revealed that hypertrophic cardiomyopathy and edematous phenotypes were highly prevalent. However, the pathophysiology and molecular mechanisms underlying NS with *RIT1* mutations remains unclear.

Added value of this study

In this study, we generated a novel NS mouse model with a *RIT1* A57G mutation. The *Rit1*$^{A57G/+}$ mice successfully replicated NS symptoms including fetal abnormalities, a short stature, craniofacial abnormalities, splenomegaly, and cardiac hypertrophy. The *Rit1*$^{A57G/+}$ mice had cardiac hypertrophy with increased cell proliferation and fibrosis in the heart without cardiomyocyte hypertrophy. Elevated expression of vimentin and periostin in the heart implied that genetic insult could exist in *Rit1*$^{A57G/+}$ mice. Furthermore, upon β–adrenergic stimulation, the heart of mice exhibited significant susceptibility to cardiac fibrosis. Although we could not identify any constitutional hyperactivation of ERK, p38, and AKT compared to wild type littermates, we observed increased phosphorylation of AKT signaling molecules in developing embryos and hearts upon β–adrenergic stimulation.

Implications of all the available evidence

These data suggest that the AKT signaling pathway may be involved in the underlying mechanism of developing NS with *RIT1* mutations. Our novel *Rit1* A57G knock-in mice are useful for investigating the mechanisms and therapeutic strategy for NS patients with *RIT1* mutations.

germline mutations in *PTPN11* occur in approximately 50% of patients with NS [10]. Subsequently, various mutations encoding RAS/MAPK pathway-related components, such as *SOS1*, *RAF1*, *KRAS*, *NRAS*, *RRAS*, *A2ML1*, *SOS2*, *LZTR1*, *PPP1CB*, *SHOC2* and *CBL*, have been found to be associated with the pathogenesis and phenotypes in NS [7,11,12]. As one of the causative genes in NS, we reported on germline mutations in *RIT1* in 2013 [13].

RIT1 (RAS-like without CAAX 1) is a member of the RAS subfamily of small GTPases and shares sequence identity with HRAS, KRAS, NRAS and RIN [14–17]. *RIT1* is ubiquitously expressed in both embryonic and adult stages [14,18]. RIT1 has been shown to contribute the growth of neuronal cells via activation of downstream effectors (p38 and AKT) [19–22]. On the other hand, a recent report showed that RIT1 functions as a regulator of actin dynamics, and increased MEK-ERK activation but not AKT activation was observed under serum stimulation in HEK293T cell line with NS-associated RIT1 mutants, such as A57G, F82L, and G95A [23]. Moreover, in our previous paper, we also demonstrated that many *RIT1* mutations found in NS patients, including S35T, A57G, E81G, F82L, and G95A, result in an increased transcription of Elk, a downstream transcription factor of ERK, in NIH 3T3 cells [13]. Taken together, these findings indicate that most NS-associated RIT1 mutations represent gain-of-function mutations; however, the downstream effector remains unclear.

When carrying these *RIT1* gain-of-function mutations, zebrafish showed craniofacial abnormalities, incomplete looping and a hypoplastic chamber in the heart. These findings suggest that RIT1 plays a significant role in development [13]. However, a mouse null for *Rit1* has been reported to survive without any pathological manifestations [24]. Additionally, an association between somatic mutations of RIT1 and cancer, including lung adenocarcinomas and myeloid malignancies, has been reported [25–28], similar to the case for other genes related to the RAS/MAPK pathway, such as *BRAF*, *HRAS* and *KRAS*. Intriguingly, the expression of RIT1 has been correlated with poor prognosis in endometrial cancer [28], whereas in esophageal squamous cell carcinoma, RIT1 was reported to predict good prognosis with suppression of the progression and metastasis of the neoplasm [29]. In summary, the function of RIT1 has remained controversial.

Genotype-phenotype analysis has shown the clinical features of NS patients with *RIT1* mutations, including higher frequencies of congenital heart diseases, wrinkled palms and soles, and lower frequencies of ptosis and short stature [30]. Among the features, a notably high prevalence of hypertrophic cardiomyopathy (HCM) has been found in NS patients with *RIT1* mutations (54%); this contrasts to a prevalence of only 20% in overall NS patients [9,30,31]. Therefore, *RIT1* is the second most frequent genes associated with HCM in NS (following *RAF1*) among previously established causative genes [30]. Nevertheless, the systemically constitutive activation of RIT1 has not been investigated. In the previous study, we found not only that *RIT1* A57G was the most common gene mutations in NS with RIT1 mutation, but also that all NS patients with *RIT1* A57G were diagnosed as HCM [13]. Thus, here we generated a knock-in mouse model that expresses the NS-associated *Rit1* A57G germline mutation. *Rit1*$^{A57G/+}$ mice developed NS-associated phenotypes, including a definitive facial appearance, short statures, splenomegaly, edema and hemorrhage. *Rit1*$^{A57G/+}$ mice also exhibited cardiac hypertrophy and cardiac fibrosis with increased fibroblast-specific protein-1 (FSP1)/S100A4, vimentin and periostin expression. Furthermore, upon β-adrenergic receptor (β-AR) stimulation, the cardiac fibrosis of *Rit1*$^{A57G/+}$ mice was exacerbated with elevated AKT phosphorylation.

2. Materials and methods

2.1. Generation of the *Rit1*$^{A57G/+}$ knock-in mouse

To construct the targeting vector to create *Rit1* A57G knock-in mice, DNA fragments that contained the *Rit1* intron 3 and exons 4–6 (including the 3′ UTR) were amplified using mouse BAC clones, and the amplified DNA products were confirmed by sequencing. The *Rit1* intronic DNA and exons 4–6 were ligated into the pBSIISK+ and pBS vectors, respectively. The *Rit1* A57G (exon 4) mutation was introduced using site-directed mutagenesis. For construct A, the previously produced SA-STOP-SV40polyA-FRT-Neo regions [32] were inserted into the pBSIISK + vector containing the *Rit1* intron. For the targeting vector, construct A fragments were inserted into the pBS+ vector containing *Rit1* exons 4–6. Bruce-4 ES cells (derived from C57BL/6 mice) were transfected with the targeting vector by electroporation, and clones were screened by Southern blot analysis for homologous recombination (data not shown). Screened ES cell clones were microinjected into BALB/c blastocysts, and the resultant chimeric mice were crossed with CAG-Cre transgenic mice on a C57BL/6J background (RIKEN BioResource Center, Tsukuba, Japan; RBRC01828) [33] to delete the SA-STOP-SV40polyA-FRT-Neo cassette via Cre-mediated recombination (Supplemental Fig. 1). The *Rit1*$^{A57G/+}$ heterozygous mice were then backcrossed with C57BL/6J mice (Charles River Laboratories Japan, Yokohama, Japan) for more than five generations.

2.2. Genotyping

DNA purification was performed as previously described [32,34]. Briefly, DNA was extracted from the tail tissue using either a DNeasy Blood & Tissue Kit (Qiagen, Hilden, Germany) or a Maxwell 16 Mouse

Tail DNA Purification Kit (Promega, Madison, WI, USA). PCR was performed using Takara PrimeSTAR HS Polymerase (Takara Bio Inc., Shiga, Japan) with the following primers: 5′-GCTGTGAATAAGATACATGAC CGACC-3′ and 5′-CCATCTCATTGGCTCCTAAGTTG-3′.

2.3. Animals

Mice were provided food and water ad libitum and were maintained under 12-h light/12-h dark cycles under specific pathogen-free conditions. The *Rit1*$^{A57G/+}$ heterozygous male mice were mated with C57BL/6J female mice that had been purchased from Charles River Laboratories Japan. In all experiments, mutant mice were compared to their wild type littermates.

Animals were sacrificed under inhaled isoflurane anesthesia. Blood samples were collected from the inferior vena cava and were subjected to blood counting by a PARTICLE COUNTER (PCE-310; ERMA, Tokyo, Japan). The rest of blood sample was collected in Capiject tubes (CJ-AS; Terumo, Tokyo, Japan) and centrifuged 6000 ×*g* for 20 min. Serum was stored in −80 °C. Biochemical analysis of serum samples was performed by Oriental Yeast Co. (Tokyo, Japan). Tissue samples were procured and immediately snap-frozen under liquid nitrogen and then stored in −80 °C.

2.4. Quantitative reverse transcription-PCR

Quantitative reverse transcription-PCR was performed as previously described [34]. Primers and hydrolysis probes are listed in Supplemental Table 1.

2.5. Western blot analysis

Lysates were prepared from tissues and Western blot analyses were performed as previously described [34]. After blocking with 5% nonfat milk in TBST (10 mmol/L Tris-HCl pH 8.0, 150 mmol/L NaCl and 0.1% Tween20) for 1 h at room temperature, the membranes were incubated with antibodies targeting the following proteins; ERK1/2 (#9102, RRID:AB_330744), phospho-ERK1/2 (#9101, RRID:AB_331646), p38 (#9212, RRID:AB_330713), phospho-p38 (#4511, RRID:AB_2139682), AKT (#9272, RRID:AB_329827), phospho-AKT at Ser473 (#9018, RRID:AB_2629283), phospho-AKT at Thr308 (#2965, RRID:AB_2255933), Vimentin (#5741, RRID:AB_10695459), phospho-MEK1/2 (Ser217/22) (#9121, RRID:AB_331648), p70S6K (#2708, RRID:AB_390722), phospho-GSKα/β (Ser21/9) (#9331, RRID:AB_329830), phospho-mTOR (Ser2448) (#5536, RRID:AB_10691552), phospho-PRAS40 (Thr246) (#2997, RRID:AB_2258110), phospho-p70S6K (Thr389) (#9234, RRID:AB_2269803), phospho-4E-BP1 (Thr37/46) (#2855, RRID:AB_560835), 4E-BP1 (#9644, RRID:AB_2097841), and GAPDH (#2118, RRID:AB_561053) (all from Cell Signaling Technology, Danvers, MA); recombinant mouse Periostin/OSF-2 (AF2955, RRID:AB_664123) from R&D Systems (Minneapolis, MN); S100A4 (#07-2274, RRID:AB_10807552) from Millipore (St Louis, MO, USA); and RIT1 (HPA053249, RRID:AB_2682089) from Sigma-Aldrich. The signals were visualized using a Western Lightning ECL-Plus Kit (PerkinElmer, Waltham, MA). The band intensities were quantified using NIH ImageJ software.

2.6. Histology and immunohistochemistry

Sections for histology and immunohistochemistry were prepared as previously described [34]. The sections were stained with picrosirius red according to standard protocols. For wheat germ agglutinin (WGA) staining, the sections were treated with a solution of FITC-conjugated WGA (L4895, Sigma-Aldrich) in PBS for 120 min at room temperature. Then, nuclei were stained with DAPI using ProLong Gold Antifade Mountant with DAPI (Thermo Fisher Scientific). The cross-sectional area of cardiomyocytes with centrally located nuclei was quantified (200–500 cells per sample) using NIH ImageJ software. Cell numbers were counted using WGA staining. All identifiable cardiomyocytes and nuclei of interstitial cells were counted in 8 to 10 randomly selected fields on the left ventricle. The counted cell numbers were divided by the area of each cardiac tissue area, and then averaged.

For immunohistochemistry, antigens were activated using a Histofine simple stain kit (Nichirei Bio Sciences, Tokyo, Japan) when necessary. Antibodies against Ki-67 (418,071, Nichirei Bio Science) or recombinant mouse Periostin/OSF-2 (AF2955) were used. The signals were visualized using a DAB Substrate Kit (Nichirei Bio Sciences). Nuclei were counterstained with hematoxylin.

To assess fibrosis, the proportion of the picrosirius-stained area in each short-axis heart section was measured using ImageJ software.

To count Ki-67-positive nuclei, three fields (236 × 177 μm per field) on the free wall of the left ventricle were randomly selected per sample, and Ki-67-positive nuclei and total nuclei were counted. The average of these values was used as the ratio per sample.

2.7. In situ hybridization

In situ hybridization of C57BL/6J embryos at E18.5 were performed as previously described [34]. The following sequence is the designed probe targeting *Rit1*:

5′-AGAGTGTGTGTACCGTGTGCACTTGACTAAGGTCACAACAGAACGT TGTGTTGTATTCTCCCCACCACCCTTCAACCTGAACTTCCTGCTACTGTCTCA CAGAAGGACATCTGCGTTGTGTAGCCACACTGTGCGTCCTGGAGACAGAG CAGAGATTGAGTAGGGAAACTGGCGTGAAAGGTGAGCAGGCGTCTGC GGAGCGGATTCCTGTGGTGGACCGTGGAGTGCAGAGGTTTAGGGAGATCC TGCCATTGCTCACACAAGAAGACAGAGCCGGAAACATGCAGGGTCAGACC AGTGTTCCTACAGTGAGCCCCAGAACTGCACATTTGACCCAAAGGCACTC AGGTGGTGAAAAGAGACAGAAGCGTATTTCTCTCTGAACATGCTTGGCTC CCCCCCCCCCCCAGTGTCTGCCTTTCTTTACCTGTGAGGCCTGGTTCTGGATC TGGGACCATTGCTGGATGACTTGAATCTTAGTGAAGTCCTTTGTTGGGCT ATGGGCT-3′.

2.8. Echocardiography

Echocardiographic experiments using Nemio35 (SSA 550A, Toshiba Medical Systems, Tokyo, Japan) were performed on mice subjected to inhalational anesthesia with isoflurane as described previously [35,36]. The data corresponding to the left ventricular dimensions and contractions were obtained from the short-axis view through parasternal space, measured for at least three proper cycles and averaged for each animal.

2.9. Catheter examination

Catheter examinations were performed in mice subjected to continuous inhalational anesthesia with isoflurane. After a mouse was fixed, the right carotid artery was incised and a Miller Mikro-Tip pressure catheter (AD Instruments Pty Ltd., Bella Vista, Australia) was inserted into the left ventricle. The pressure wave was recorded and analyzed using LabChart8 (AD Instruments Pty Ltd.). All variables were measured over five cycles and averaged for each animal.

2.10. Drug administration

Mini osmotic pumps (Model 1004 pump, ALZET Tech, Cupertino, CA), containing either ISO (10 mg/kg/day) (Sigma-Aldrich) in normal saline (Otsuka, Tokyo, Japan) or normal saline alone were subcutaneously implanted in the backs of 11-week-old mice subjected to inhalational anesthesia with isoflurane. These mice were sacrificed after 7 days of treatment.

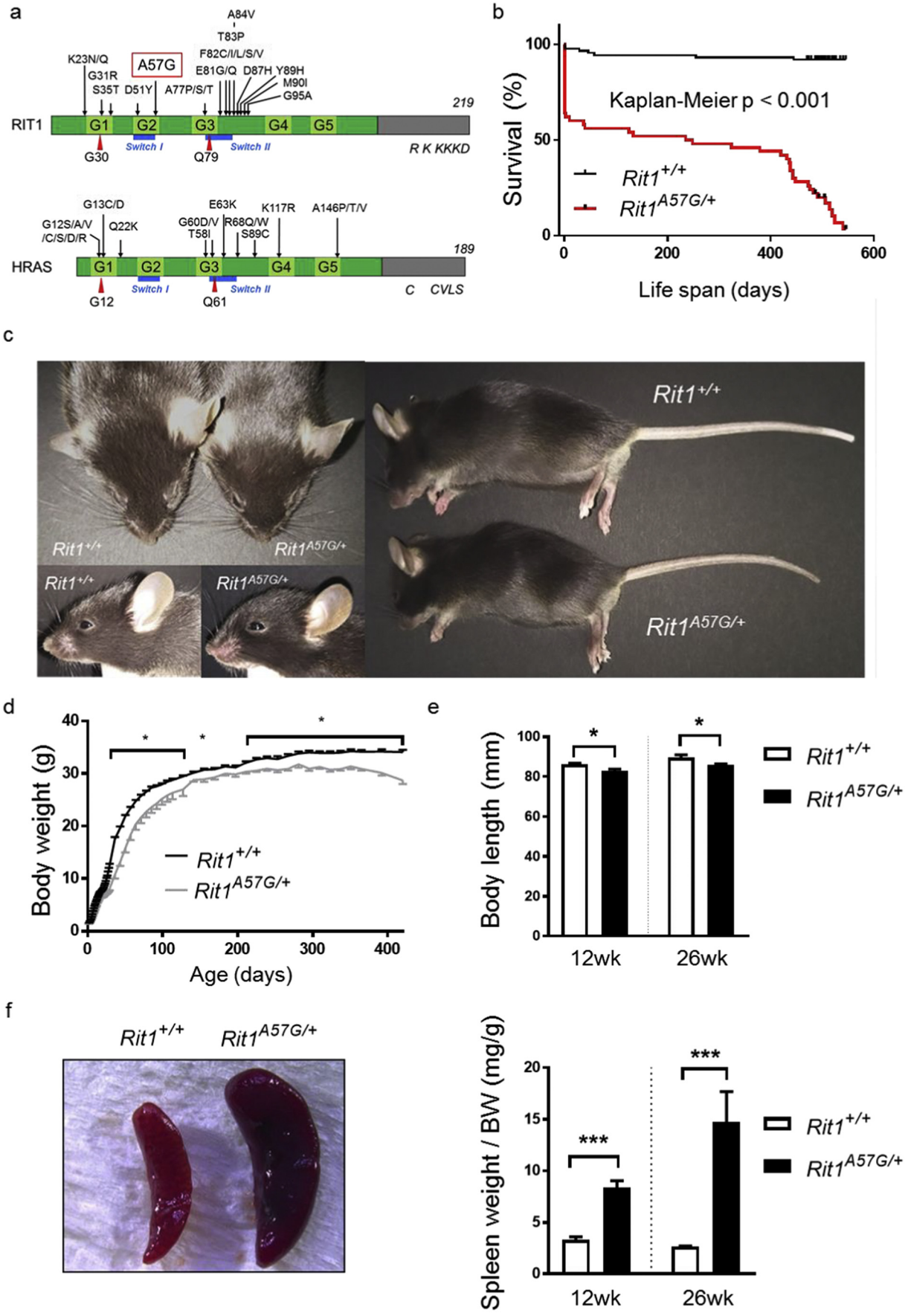
a
A84V
T83P
F82C/I/L/S/V
K23N/Q
A57G
E81G/Q D87H Y89H
G31R
M90I
S35T D51Y A77P/S/T
G95A
219
RIT1
G1 G2 G3 G4 G5
Switch I
Switch II
G30
Q79
R K KKKD
G13C/D
E63K
K117R
A146P/T/V
G12S/A/V
/C/S/D/R
Q22K
G60D/V
T58I
R68Q/W
S89C
189
HRAS
G1 G2 G3 G4 G5
Switch I
Switch II
G12
Q61
C CVLS
b
Survival (%)
Kaplan-Meier p < 0.001
Rit1+/+
Rit1A57G/+
Life span (days)
c
Rit1+/+
Rit1A57G/+
Rit1+/+
Rit1A57G/+
Rit1+/+
Rit1A57G/+
d
Body weight (g)
Rit1+/+
Rit1A57G/+
Age (days)
e
Body length (mm)
Rit1+/+
Rit1A57G/+
12wk
26wk
f
Rit1+/+
Rit1A57G/+
Spleen weight / BW (mg/g)
Rit1+/+
Rit1A57G/+
12wk
26wk

2.11. Statistical analysis

All statistical analyses were performed using Prism version 7.04 (GraphPad Inc., Lo Jolla, CA). Comparisons between two groups were performed using either the unpaired Student's *t*-test or the Mann-Whitney test as appropriate, and comparisons among three or more groups were performed with one-way ANOVA followed by the Tukey-Kramer post hoc test when the ANOVA results were significant. For body weight, two-way ANOVA followed by the Sidak multiple comparisons test as a post hoc test was used. Survival was analyzed with the Kaplan-Meier method with the log-rank test. *P*-values are expressed as $^{*}p < .05$, $^{**}p < .01$, $^{***}p < .001$.

2.12. Study approval

All animal experiments were approved by the Animal Care and Use Committee of Tohoku University (2018MdA-090, 2018MdA-022), which conforms NIH guidelines (Guide for the Care and Use of Laboratory Animals, Eighth Edition).

3. Results

3.1. Generation of Rit1 A57G knock-in mice

RIT1 belongs to the RAS subfamily and shares its construction with other RAS subfamily proteins such as HRAS, although RIT1 does not have a carboxy-teminal CAAX motif, which targets the protein to the plasma membrane (Fig. 1a) [37]. A57 is located in the switch I region, which plays an important role in the hydrolysis of GTP (Fig. 1a) [38,39]. Previously, we have reported that enhanced transcription levels of ELK1 were observed in NIH 3 T3 cells with RIT1 A57G [13], which indicates that RIT1 A57G is a gain-of-function mutation. To investigate the gain-of-function mutation of RIT1 A57G, which is one of the most frequent mutations in NS patients [13,30], we generated *Rit1* A57G knock-in mice as an NS model according to the strategy mentioned in the methods section (see Methods 2.1). PCR of genomic DNA extracted from a tail tip was performed routinely to determine the genotypes of the prenatal and postnatal mice (Supplemental Fig. 2).

We firstly confirmed that *Rit1* was ubiquitously expressed in C57BL/6J mouse tissues using in situ hybridization and Western blotting (Supplemental Figs. 3 and 4) [14]. In the heart tissues of embryo and adult C57BL/6J mouse, *Rit1* was also expressed in cardiomyocytes and interstitial cells, including endothelial cells and cardiac fibroblasts (Supplemental Fig. 3d and i).

Male $Rit1^{A57G/+}$ mice were fertile, while female $Rit1^{A57G/+}$ mice had remarkably low reproductive ability (data not shown). At weaning, the $Rit1^{A57G/A57G}$ mice were not procured, and the number of $Rit1^{A57G/+}$ mice was lower than the anticipated Mendelian ratio (30 of 115; 26.1%) (Table 1). Therefore, we investigated the longevity of the $Rit1^{A57G/+}$ mice after delivery. Of note, approximately half of the $Rit1^{A57G/+}$ mice died within two days after birth (Fig. 1b). After weaning, most $Rit1^{A57G/+}$ mice survived until 400 days; thereafter, the $Rit1^{A57G/+}$ mice succumbed earlier than the $Rit1^{+/+}$ mice. However, we could not identify the cause of death. Subsequently, we investigated the progeny ratio of these genotypes during development. A reduced Mendelian ratio of the $Rit1^{A57G/+}$ mice was observed at E13.5, E16.5, E18.5 and at birth (Table 1). Most homozygous $Rit1^{A57G/A57G}$ mice that were obtained from intercrossing $Rit1^{A57G/+}$ heterozygous mice showed prenatal lethality. To investigate the cause of pre- and postnatal death, we examined the phenotypes of embryos. Six of the 45 live $Rit1^{A57G/+}$ embryos at E16.5 showed severe fetal hydrops and significant subcutaneous hemorrhage (Supplemental Fig. 5). However, we did not detect any cardiovascular abnormalities, including pulmonary stenosis or atrioventricular septal defects, in the $Rit1^{A57G/+}$ mice (data not shown). RIT1 has been reported to activate ERK, p38 and AKT signaling in murine embryonic fibroblasts, neuronal cells and cancer cells [24,26,40]. To assess the effect of the *Rit1* A57G mutation on the RAS/MAPK and AKT signaling pathways during development, whole-cell lysates of $Rit1^{+/+}$, and $Rit1^{A57G/+}$ embryos at E13.5 were immunoblotted. Although the levels of phosphorylated ERK and p38 did not alter between genotypes, the levels of AKT phosphorylated at Thr308, GSK 3α/β phosphorylated at Ser21/9, and p70S6K phosphorylated at Thr389 were significantly higher in the $Rit1^{A57G/+}$ embryos than in the $Rit1^{+/+}$ embryos (Supplemental Fig. 6). Taken together, these findings show that although the cause of embryonic or neonatal death in the $Rit1^{A57G/+}$ and $Rit1^{A57G/A57G}$ mice remains unclear, the *Rit1* A57G mutation might activate the AKT signaling pathway during fetal development.

Table 1
The progeny ratio of *Rit1* A57G embryos and neonates.

A

$Rit1^{+/+}\times Rit1^{A57G/+}$	E13.5	E16.5	E18.5	P0	Weaning
$Rit1^{+/+}$	19 (63.3%)	40 (56.3%)	21 (61.8%)	88 (65.2%)	85 (73.9%)
$Rit1^{A57G/+}$	11 (36.7%)	31 (43.6%)	13 (38.2%)	47 (34.8%)	30 (26.1%)
Total	30	71	34	135	115

B

$Rit1^{A57G/+}\times Rit1^{A57G/+}$	E13.5	E16.5	E18.5	Weaning
$Rit1^{+/+}$	13 (36.1%)	8 (22.9%)	4 (33.3%)	6 (54.5%)
$Rit1^{A57G/+}$	17 (47.2%)	24 (68.6%)	7 (58.3%)	5 (45.5%)
$Rit1^{A57G//A57G}$	6 (16.7%)	1 (2.9%)	1 (8.3%)	0
Total	36	35	12	11

3.2. $Rit1^{A57G/+}$ mice show facial dysmorphia, small body size, and splenomegaly

Adult $Rit1^{A57G/+}$ mice exhibited a short stature and distinctive facial appearance, including a round head and a short nose, similar to that observed in other murine models of RASopathies (Fig. 1c) [32,35,36,41–44]. The male $Rit1^{A57G/+}$ mice had a significantly lower body weight (BW) than that of the $Rit1^{+/+}$ mice, whereas the BW of the female $Rit1^{A57G/+}$ mice was almost the same as that of the $Rit1^{+/+}$ mice, except for a short periods between 3 and 12 weeks old and between 52 and 60 weeks old (Fig. 1d and Supplemental Fig. 7). Furthermore, the male $Rit1^{A57G/+}$ mice exhibited significantly shorter body length than their $Rit1^{+/+}$ littermates at 12 and 26 weeks old (Fig. 1e). Interestingly, most of the $Rit1^{A57G/+}$ mice (22 of 24) had rectal prolapse at 1 year old, whereas no rectal prolapse was observed in their $Rit1^{+/+}$ littermates (Supplemental Fig. 8). Of note, the $Rit1^{A57G/+}$ mice exhibited a remarkable increase in spleen size reminiscent of other NS mouse models (Fig. 1f) [41,44], although histological analysis showed that there was no obvious constructional change and monoclonal proliferation (Supplemental Fig. 9a). Cell blood counts revealed that the

Fig. 1. General features of the $Rit1^{A57G/+}$ mice. a, Structure and identified germline alterations in RIT1 and HRAS. b, Survival curve of $Rit1^{+/+}$ ($n = 87$) and $Rit1^{A57G/+}$ ($n = 58$) mice assessed using the Kaplan-Meier method. c, Representative images of $Rit1^{+/+}$ and $Rit1^{A57G/+}$ male mice at 6 weeks old. $Rit1^{A57G/+}$ mice have a shortened nose, round head, and stunted growth. d, Body weight was measured every day from birth to 28 days, once per week from 4 to 16 weeks, and once every couple of weeks from 18 to 52 weeks ($n = 39$ and 27 in $Rit1^{+/+}$ and $Rit1^{A57G/+}$ males, respectively). Data are presented as means ± SEM. $^{*}p < .05$ with two-way ANOVA followed by Sidak multiple comparisons test. e, Body length was measured at 12 and 26 weeks (n = 8 per group). Data are presented as means ± SEM. $^{**}p < .01$, $^{***}p < .001$ using the Mann-Whitney test. f, Representative image of spleen from $Rit1^{+/+}$ and $Rit1^{A57G/+}$ male mice at 12 weeks. Spleen weight/body weight were compared between the genotypes at 12 and 26 weeks old (n = 8 per group). Data are presented as means ± SEM. $^{*}p < .05$, $^{**}p < .01$ using the Mann-Whitney test.

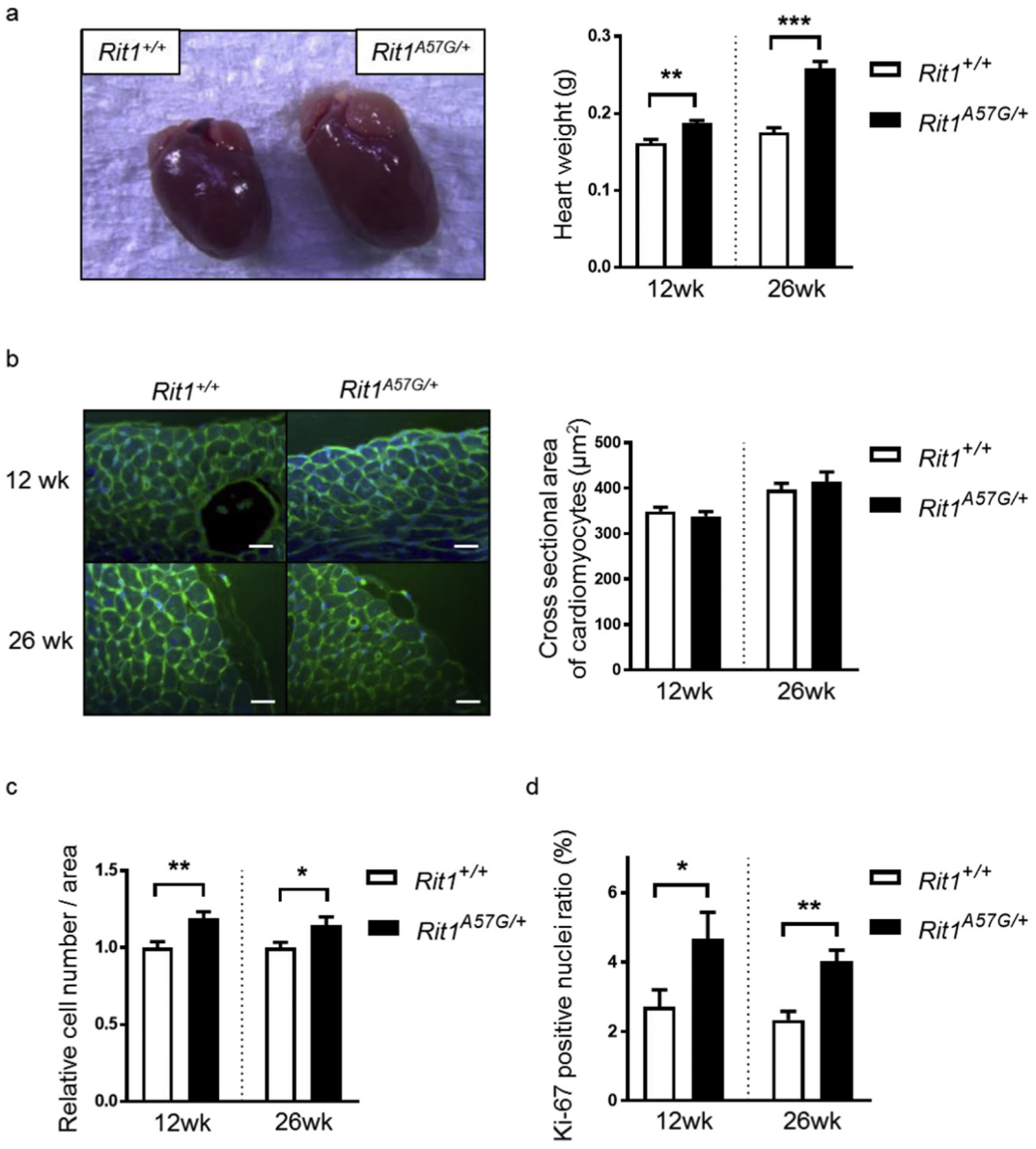

Fig. 2. *Rit1*$^{A57G/+}$ mice have cardiomegaly but do not have cardiomyocyte hypertrophy or cardiac failure. a, Representative gross images of the hearts of *Rit1*$^{+/+}$ and *Rit1*$^{A57G/+}$ mice. Heart weights were compared between *Rit1*$^{+/+}$ and *Rit1*$^{A57G/+}$ mice at 12 and 26 weeks (n = 8 in each group). b, Wheat germ agglutinin staining of the sections from *Rit1*$^{+/+}$ and *Rit1*$^{A57G/+}$ mice at 12 and 26 weeks. Original magnification × 200. Scale bar: 200 μm. The cross-sectional area of cardiomyocytes from the left ventricles was measured (*Rit1*$^{+/+}$: *Rit1*$^{A57G/+}$, n = 8:7 at 12 weeks, n = 8:8 at 26 weeks old) and compared between *Rit1*$^{+/+}$ and *Rit1*$^{A57G/+}$ mice. c, Relative cell numbers per area were compared between *Rit1*$^{+/+}$ and *Rit1*$^{A57G/+}$ mice at 12 and 26 weeks. d, Ki-67-positive nuclei and total nuclei were counted in three random fields (945 × 708 μm/field) on the left ventricular wall. The ratios of Ki-67-positive nuclei and total nuclei were averaged for each mouse. The averaged ratios were compared between the genotypes at 12 and 26 weeks (n = 8, in each group). Data are presented as means ± SEM. *p < .05, **p < .01, ***p < .001 using the Mann-Whitney test.

Rit1$^{A57G/+}$ mice had significant anemia at 26 weeks old (Supplemental Fig. 9b and 9c); however, unlike reported mouse models of NS, there was no significant increase in the number of white blood cells in the *Rit1*$^{A57G/+}$ mice (Supplemental Fig. 9d) [41,44]. Biochemical analysis revealed that although *Rit1*$^{A57G/+}$ mice had elevated aspartate transaminase at 26 weeks of age, other markers for hepatic, renal, and metabolic function did not alter significantly (Supplemental Table 2). Furthermore, there were no differences in anatomical features of lung, liver and kidney between *Rit1*$^{+/+}$ and *Rit1*$^{A57G/+}$ mice at 12, 26 or 52 weeks of age (data not shown).

3.3. *Rit1*$^{A57G/+}$ mice have cardiac hypertrophy with increased proliferation, but no functional decline

Approximately one half of NS patients with *RIT1* mutations develops HCM [30]. We therefore focused on the cardiac phenotype in the *Rit1*$^{A57G/+}$ mice. At 12 and 26 weeks old, the *Rit1*$^{A57G/+}$ mice had a significantly heavier heart weight (HW) and a higher HW/BW ratio than the *Rit1*$^{+/+}$ mice (Fig. 2a and Supplemental Fig. 10). Echocardiographic analysis revealed that the *Rit1*$^{A57G/+}$ mice had a relatively thickened left ventricular wall when compared to the *Rit1*$^{+/+}$ mice (Table 2). In a cardiac catheter examination, cardiac contractility ($+dP/dt$ and $-dP/dt$) was comparable between the *Rit1*$^{+/+}$ and *Rit1*$^{A57G/+}$ mice at 28 weeks old (Supplemental Table 3). Furthermore, there were no differences in mRNA expression levels of markers of cardiac failure between the *Rit1*$^{+/+}$ and *Rit1*$^{A57G/+}$ mice (Supplemental Fig. 11). Histological analysis revealed that the average size of the cardiomyocytes obtained from the *Rit1*$^{A57G/+}$ mice at 12 and 26 weeks old was comparable to that of cardiomyocytes obtained from the *Rit1*$^{+/+}$ mice (Fig. 2b). However, heart sections from the *Rit1*$^{A57G/+}$ mice had a higher number of cells, including cardiomyocytes, cardiac fibroblasts and endothelial cells (Fig. 2c). Additionally, Ki-67 staining

Table 2
Echocardiographic parameters in *Rit1*$^{+/+}$ and *Rit1*$^{A57G/+}$ mice.

12 weeks	*Rit1*$^{+/+}$ (n=8)	*Rit1*$^{A57G/+}$ (n=8)	p-value
IVSTd, mm	0.797 ± 0.096	0.834 ± 0.143	0.3998
PWTd, mm	0.690 ± 0.322	0.683 ± 0.125	0.9581
LVDd, mm	3.519 ± 0.425	3.940 ± 0.482	0.0520
LVDs, mm	2.410 ± 0.247	2.702 ± 0.321*	0.0313
LVEF	0.692 ± 0.035	0.664 ± 0.039	0.3006
LVFS	0.337 ± 0.027	0.316 ± 0.028	0.1278
26 weeks	*Rit1*$^{+/+}$ (n=8)	*Rit1*$^{A57G/+}$ (n=6)	p-value
IVSTd, mm	0.786 ± 0.149	0.814 ± 0.138	0.5177
PWTd, mm	0.513 ± 0.096	0.653 ± 0.038*	0.0234
LVDd, mm	4.109 ± 0.506	4.278 ± 0.556	0.4772
LVDs, mm	3.078 ± 0.571	3.047 ± 0.498	1.0000
LVEF	0.562 ± 0.088	0.626 ± 0.045	0.1376
LVFS	0.253 ± 0.052	0.292 ± 0.026	0.1376

Data are presented as the means ± SD. *$p < 0.05$ using the Student's *t*-test. IVSTd, interventricular septum thickness in diastole; LVDd, left ventricular end-diastolic dimension; LVDs, left ventricular end-systolic diameter; LVEF, left ventricular ejection fraction; LVFS, left ventricular fractional shortening; PWTd, posterior wall thickness in diastole.

showed a higher proliferation rate in heart tissue at 12 and 26 weeks old (Fig. 2d and Supplemental Fig. 12).Taken together, these data indicate that the *Rit1*$^{A57G/+}$ mice have cardiac hypertrophy and increased cell proliferation, but not cardiomyocyte size, without a deterioration of heart function.

3.4. *Rit1*$^{A57G/+}$ mice have elevated expression levels of S100A4, periostin and vimentin in heart

Further histological analysis of the hearts revealed that the *Rit1*$^{A57G/+}$ mice had a significantly higher proportion of collagen accumulation than that in the *Rit1*$^{+/+}$ mice at 12 and 26 weeks old (Fig. 3a). To examine if cardiac fibrosis and increased cell proliferation observed in *Rit1*$^{A57G/+}$ mice are caused by increased cell proliferation of cardiac fibroblasts, S100A4, a fibrotic marker, was assessed by immunostaining. The numbers of S100A4-positive cells in *Rit1*$^{A57G/+}$ mice increased compared with *Rit1*$^{+/+}$ mice at 6 weeks of age (Fig. 3b). Moreover, immunostaining showed that periostin, which has recently been recognized as a marker of activated cardiac fibroblasts and myofibroblasts [45] as well as a factor involved in cardiac remodeling [46], was induced in both the endocardial and perivascular areas of the *Rit1*$^{A57G/+}$ mice (Fig. 3c). Furthermore, the mRNA expression levels of fibrotic markers in the left ventricle, including *Vim*, *Postn*, *S100a4* and *Col1a1* were increased in 12- and/or 26-week-old mice in the *Rit1*$^{A57G/+}$ mice (Fig. 3d). Immunoblots of lysates from the left ventricle confirmed the increased levels of S100A4, vimentin and periostin in the *Rit1*$^{A57G/+}$ mice at 12 and/or 26 weeks (Fig. 3e and Supplemental Fig. 13). In contrast, no changes in the phosphorylation status of ERK1/2, p38, and AKT, which have been supposed to be involved in the mechanisms of RASopathies, were observed (Supplemental Fig. 14). These data suggest that cardiac fibroblasts and myofibroblasts were proliferating or activated in the *Rit1*$^{A57G/+}$ mice, which resulted in a pronounced fibrotic change that was accompanied by increased expressions of S100A4, periostin and vimentin.

3.5. β-adrenergic stimulation exacerbates pathological fibrosis in *Rit1*$^{A57G/+}$ mice

As shown above, the *Rit1*$^{A57G/+}$ mice presented with cardiac hypertrophy with increased proliferation, and a higher rate of fibrotic tissue accumulation, which was accompanied by increased expressions of S100A4, vimentin and periostin. Therefore, we hypothesized that the *Rit1*$^{A57G/+}$ mice might be susceptible to sympathetic nervous stimulation with isoproterenol (ISO), which leads to cardiac fibrosis and cardiac hypertrophy in mice [47]. ISO (10 mg/kg/day) administration (Fig. 4a) increased the HW/BW ratio in both genotypes when compared to their respective vehicle groups (Fig. 4b). The cross-sectional area of cardiomyocytes was also increased in both genotypes, although the increase did not reach statistical significance (Supplemental Fig. 15). Consistent with other reports [48,49], the percentages of fibrosis area in the hearts from saline-treated *Rit1*$^{+/+}$ and *Rit1*$^{A57G/+}$ mice were higher (0.41 ± 0.10 and 0.59 ± 0.10, respectively) (Fig. 4c), than those in non-treated *Rit1*$^{+/+}$ and *Rit1*$^{A57G/+}$ mice (0.17 ± 0.04 and 0.38 ± 0.04) (Fig. 3a), suggesting a slight increase of cardiac fibrosis due to saline. ISO treatment in the *Rit1*$^{+/+}$ mice increased the area (2.50-fold) of cardiac fibrosis compared with that of saline-treated *Rit1*$^{+/+}$ mice, although there was no statistically significant difference. Meanwhile, cardiac fibrosis in the *Rit1*$^{A57G/+}$ mice was dramatically increased (10.35-fold) compared with saline-treated *Rit1*$^{A57G/+}$ mice (Fig. 4c). Immunostaining demonstrated that periostin-positive cells and interstitial space were apparently increased (Fig. 4d), suggesting that cardiac fibroblasts were significantly activated by ISO administration. Moreover, qPCR revealed that the mRNA expression levels of genes associated with heart failure and cardiac fibrosis were higher than those in the vehicle group (Supplemental Fig. 16). Immunoblots illustrated that the protein expression levels of vimentin and periostin and the phosphorylation of AKT at Thr308 were remarkably increased by ISO stimulation in the *Rit1*$^{A57G/+}$ mice when compared to the *Rit1*$^{+/+}$ mice (Fig. 4e and f; Supplemental Fig. 17). However, there were no differences in the downstream effectors of AKT, including GSK3α/β, p70S6K, proline-rich AKT1 substrate 1 (PRAS40), and eukaryotic translation initiation factor 4E-binding protein 1 (4E-BP1) in the *Rit1*$^{+/+}$ and *Rit1*$^{A57G/+}$ mice (Supplemental Fig. 18). These data suggest that β-AR stimulation exacerbates cardiac fibrosis in the *Rit1*$^{A57G/+}$ mice and that AKT phosphorylation might be involved in the development of cardiac fibrosis.

4. Discussion

Germline mutations in *RIT1* account for approximately 5–9% of mutations in NS patients [13,30]. In our previous study, we found that NS patients with a *RIT*1 mutation showed a high incidence of HCM and perinatal abnormalities (including nuchal translucency and fetal hydrops) compared to NS patients with other gene mutations [30]. In this study, we generated a mouse model expressing the *Rit1* A57G mutation; these mice presented with a short stature, craniofacial abnormalities, a reduced life span and splenomegaly, which partly recapitulate the phenotypes of NS [6,8,9,31]. The *Rit1*$^{A57G/+}$ mice also showed cardiac hypertrophy and mild cardiac fibrosis with increased expression of the fibroblast and activated fibroblast markers, S100A4, vimentin and periostin, which were partly exacerbated under β-adrenergic stimulation.

Cardiac hypertrophy, an increased number of cells and accumulation of collagen, but not cardiomyocyte hypertrophy, were observed in the *Rit1*$^{A57G/+}$ mice. In this study, we also found elevated expressions of S100A4, vimentin and periostin in the cardiac tissue of the *Rit1*$^{A57G/+}$ mice. Recent studies have shown that in the adult heart, resident cardiac fibroblasts are activated and differentiated to myofibroblasts in response to stress insults, such as inflammation, genetic factors, and pressure and volume loading [50,51]. Under such cardiac injuries, myofibroblasts accompanied by inflammatory cell accumulation and cardiomyocyte death leads to increased expressions of vimentin and periostin [52]. Of note, the *Rit1*$^{A57G/+}$ mice exhibited increased expressions of vimentin and periostin in the heart even without any additional stresses. Furthermore, β-AR stimulation lead to a dramatic worsening of cardiac fibrosis in the *Rit1*$^{A57G/+}$ hearts with increased expressions of vimentin and periostin. These observations suggest that the number of activated fibroblasts, which lead to cardiac fibrosis, was increased in the *Rit1*$^{A57G/+}$ heart and that sympathetic nervous stimulation added to the genetic insulation might be one of the triggers for the pathological changes in the heart of the *Rit1*$^{A57G/+}$ mice. Indeed, the pathological features of the heart in NS patients are consistent with these findings.

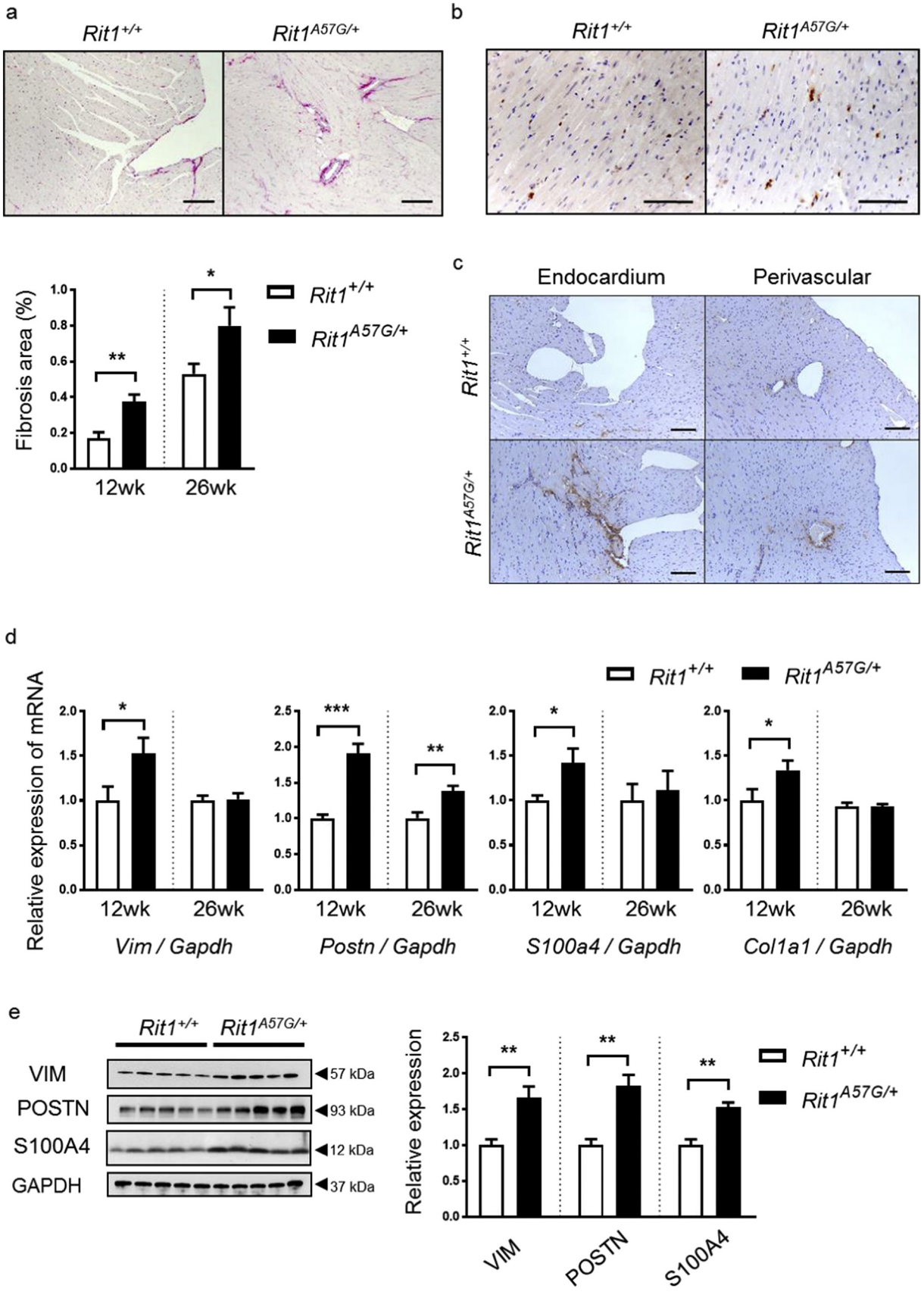

Fig. 3. *Rit1*$^{A57G/+}$ mice exhibit increased cardiac expression of the activated fibroblast markers, S100a4, periostin and vimentin. a, Representative images of heart sections stained with picrosirius red at 12 weeks. Scale bar represents: 100 μm. Fibrosis area was quantified and compared between *Rit1*$^{+/+}$ and *Rit1*$^{A57G/+}$ mice at 12 and 26 weeks (n = 8, in each group). b, Representative images of heart sections at 6 weeks subjected immunochemical staining with an anti-S100A4 antibody. Scale bar: 100 μm. c, Representative images of heart sections stained with an anti-periostin antibody. Scale bar: 100 μm. d, Relative mRNA expression of fibrosis-related markers, including *Vim*, *Postn*, *S100a4*, and *Col1a1*, in the left ventricle. The mRNA levels were normalized to those of *Gapdh* (n = 8 in each group). e, Lysates from the left ventricles were subjected to immunoblotting with the indicated antibodies (n = 5 in each group). GAPDH indicates the loading control. VIM, vimentin; POSTN, periostin. Band intensities were quantified and compared between *Rit1*$^{+/+}$ and *Rit1*$^{A57G/+}$ mice at 26 weeks. Expression levels were normalized to GAPDH. Data are presented as means ± SEM. *p < .05, **p < .01, ***p < .001 using the Mann-Whitney test.

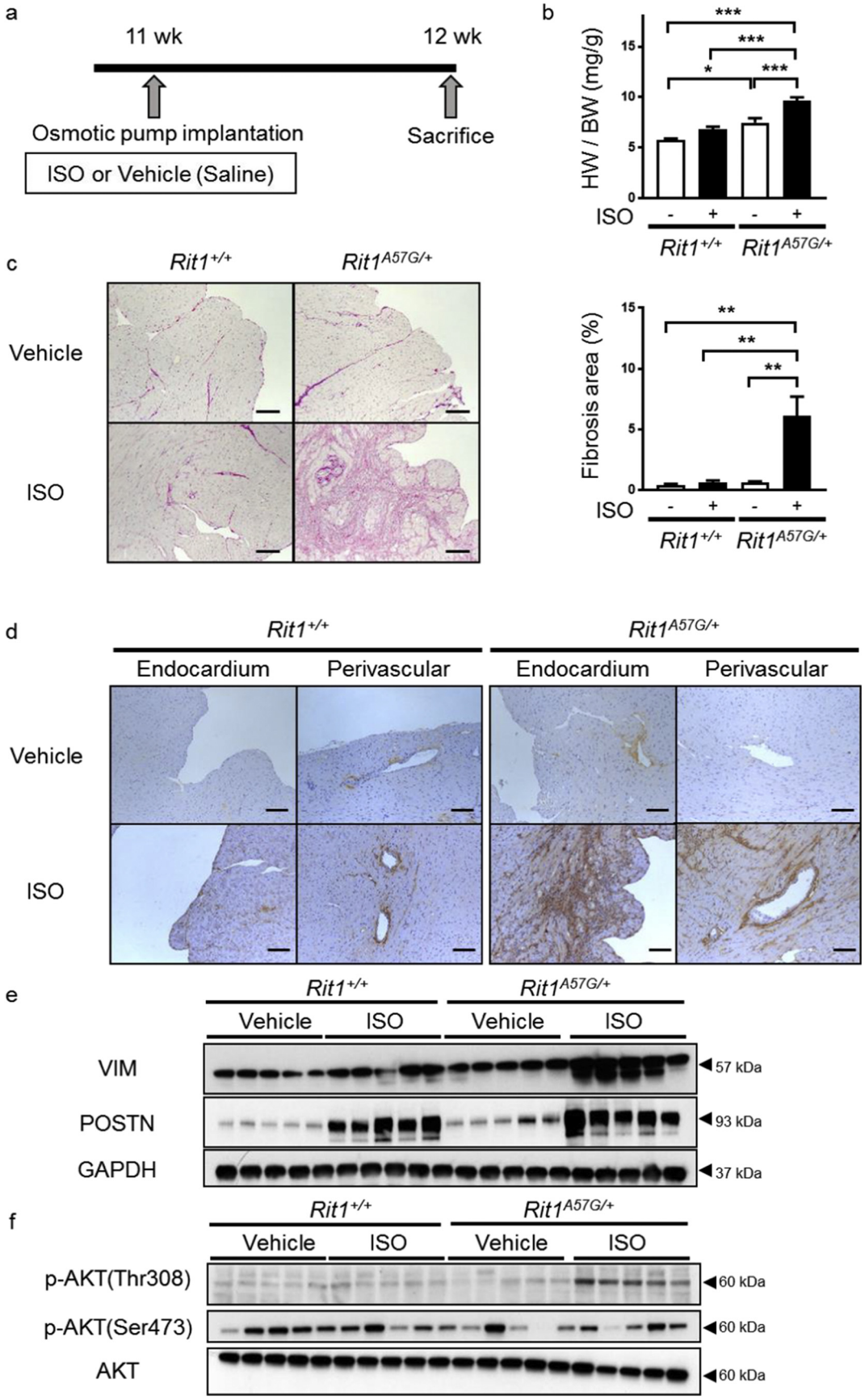

Fig. 4. Isoproterenol (ISO) administration leads to cardiac fibrosis and increased p-AKT (Thr308) levels in *Rit1*$^{A57G/+}$ mice. a, Schematic diagram of the ISO administration model. After administration of ISO for seven days, the mice were sacrificed at 12 weeks and analyzed. b, Heart weight per body weight (HW/BW) ratios were compared between the groups. (*Rit1*$^{+/+}$ with vehicle group; n = 5, *Rit1*$^{+/+}$ with ISO loading group; $n = 6$, *Rit1*$^{A57G/+}$ with vehicle group; n = 5, *Rit1*$^{A57G/+}$ with ISO loading group; $n = 7$). c, Representative images of heart sections stained with picrosirius red. Scale bar: 100 μm. The percentage of fibrosis in sections from the heart was measured and compared between the groups. d, Representative images of heart sections immunostained with the antibody against periostin. e and f, Lysates from the left ventricles were subjected to immunoblot analysis using antibodies against the indicated fibrosis-related proteins (vimentin (VIM), and periostin (POSTN)) in e and AKT and its phosphorylated forms in f. GAPDH indicates the loading control.

Hirsch et al. reported two infant cases of NS with hypertrophic obstructive cardiomyopathy with fibrosis: one patient showed fibrotic changes in the anterior papillary muscle, and the other presented with myocardial fibrosis [53]. Poterucha et al. reported that the endocardium of NS patients had a greater fibrosis score than that of non-NS patients, whereas cardiomyocyte hypertrophy was mild [54]. These reports on heart histology in NS patients suggest that in NS patients, heart tissues are susceptible to fibrosis associated with or without cardiomyocyte hypertrophy. Taken together, the findings related to the hearts of our novel *Rit1* mutant mice successfully replicated the histological features of NS patients, and this mouse model might be useful for investigations related to the treatment strategy for HCM in NS patients with a *RIT1* mutation.

The relationship between the downstream pathways of the RIT1 mutation and cardiac fibrosis and cardiac hypertrophy remains unclear. We observed increased expression of phosphorylated AKT (Thr308), p70S6K (Thr389), and GSK3α/β (Ser21/9), but phosphorylated ERK or phosphorylated p38 were not increased in the $Rit1^{A57G/+}$ whole embryos. β-AR stimulation has been known to activate AKT signaling pathway and ERK in murine heart [55]. In this study, ISO treatment increased AKT phosphorylation at Thr308, but not ERK phosphorylation, in the $Rit1^{A57G/+}$ hearts. These results suggest that the *Rit1* A57G mutation preferentially affects the AKT/mTOR pathway rather than the MEK/ERK and p38 pathways. A plethora of evidence suggests that AKT could play an important role in developing cardiac hypertrophy and fibrosis. Indeed, myocardium-specific transgenic mice expressing AKT have cardiac hypertrophy with increased cardiomyocyte size [56,57]. In terms of cardiac fibrosis, Lian et al. reported that the AKT/mTOR/p70S6K pathway is associated with heart interstitial fibrosis induced by heparin-binding EGF-like growth factor [58]. Recently, it has been also reported that the activation of PI3K/AKT, RAS/MAPK, Smad and β-catenin by mechanical stress, chemokines and changes in matrix composition induces the expression and secretion of periostin in cardiac cells of mesenchymal origin. Afterward, periostin interacts with tenascin-C and matrix-associated lysyl oxidase to stimulate $\alpha_v\beta_1$, β_3 and β_5 integrin signaling pathway. Further stimulation of PI3K/AKT and RAS/MAPK signaling due to these complexes finally leads to profibrotic phenotype [59]. This line of evidence suggests that the activation of AKT/mTOR pathway due to ISO stimulation might be responsible for the cardiac hypertrophy and pronounced fibrosis in the $Rit1^{A57G/+}$ mice. Further studies will be necessary to elucidate whether the $Rit1^{A57G/+}$ mice have increased AKT activity in cardiac fibroblast and/or cardimyocytes and, if so, whether the inhibition of AKT signaling ameliorates the cardiac phenotype in $Rit1^{A57G/+}$ mice.

The AKT/mTOR pathway has also been identified as the key cascade of the pathophysiology in patients and in mouse models of Noonan syndrome with multiple lentigines syndrome (NSML), which is one of the RASopathies. In a mouse model of NSML, *Ptpn11* Y279C mice have been reported to present with HCM with increased levels of phosphorylated AKT, p70S6K and S6 ribosomal protein [43,60]. In the report, treatment with rapamycin, an inhibitor of mTOR, or ARQ092, an AKT inhibitor, ameliorated HCM in mice expressing the *Ptpn11* Y279C mutation. Additionally, cardiomyocyte-specific transgenic mice expressing the *Ptpn11* Q510E mutation have been found to exhibit cardiomegaly and a hyperactivated AKT/mTOR pathway, and this was prevented by treatment with rapamycin [61]. Additionally, Hahn et al. reported that mTOR inhibition with everolimus, a rapamycin analog, prevents progressive HCM in NSML patients carrying the *PTPN11* Q510E mutation, whose cardiac fibroblasts showed increased phosphorylations of AKT and S6RP [62]. In this study, the gain-of-function mutation *Rit1* A57G was shown to activate the AKT/mTOR pathway during the development and under cardiac load. Thus, inhibition of the AKT/mTOR pathway might be a candidate treatment for HCM in NS patients with a *RIT1* mutation as well as in mice or individuals with NSML.

Approximately 25% of pediatric NS patients have been reported to present some degree of hepatosplenomegaly. Fewer NS patients develop a benign myeloproliferative disorder that regresses spontaneously in most cases [44]. In $Ptpn11^{D61G/D61G}$ and $K\text{-}Ras^{V41I}$ mice, which have NS-associated gene mutations, white blood cell proliferation was observed [63,64]; in contrast, our $Rit1^{A57G/+}$ mice did not show an evident proliferation of white blood cells at 12 and 26 weeks. Meanwhile, the $Rit1^{A57G/+}$ mice showed significant anemia at 26 weeks. However, platelet counts were comparable between the genotypes (data not shown); thus, it is unclear whether or not the hypersplenism caused anemia in the $Rit1^{A57G/+}$ mice.

In conclusion, we generated a novel knock-in $Rit1^{A57G/+}$ mouse that presents features that are relevant to NS patients with a *Rit1* mutation, including craniofacial dysmorphia, short stature, and cardiac hypertrophy. The hearts of the $Rit1^{A57G/+}$ mice showed cardiac hypertrophy and fibrosis with elevated expression levels of S100A4, vimentin and periostin. Furthermore, the $Rit1^{A57G/+}$ mice are remarkably susceptible to sympathetic nervous stimulation and develop significant cardiac fibrosis. Although the precise mechanisms remain unclear, the AKT/mTOR pathway might be involved in the development of the pathology resulting from RIT1 A57G mutation. Our mice might be useful to understanding the mechanism underlying the pathology of NS patients with a RIT1 mutation and in seeking a therapeutic clue for their pathology.

Acknowledgments

We wish to offer appreciation to Taiki Abe, PhD. for technical advises, and to Riyo Takahashi, Kumi Kato and Yoko Tateda for their technical assistance. We would also like to thank Kenji Yoshihara and Hiroaki Nagao at Heart Center, Tokyo Women's Medical University for their technical assistance.

Sources of funding

This work was supported by the Grants-in-Aid by the Practical Research Project for Rare/Intractable Diseases from the Japan Agency for Medical Research and Development, AMED to YA (18ek0109241h0002), by the Japan Society for the Promotion of Science (JSPS) KAKENHI Grant Number 17H04223 to YA, and by JSPS KAKENHI Grant Number 15K19598 and 18K07811 to SI, by Miyata Cardiac Research Promotion Foundation to SI, and by the Takeda Science Foundation to SI. The funders had no role in study design, data collection, data analysis, interpretation and writing of the report.

Declaration of interests

The authors have declared that no conflict of interest exists.

Author contributions

ST, SI, KM, YS and YA designed the study. ST and SI conducted experiments. YN performed echocardiography. ST, SI, SM-T, KM, YN and YA performed data analysis. ST, SI and YA wrote the initial draft of the paper. All authors reviewed and edited the manuscript.

Appendix A. Supplementary data

Supplementary data to this article can be found online at https://doi.org/10.1016/j.ebiom.2019.03.014.

References

[1] Barbacid M. ras genes. Annu Rev Biochem 1987;56:779–827.
[2] Malumbres M, Barbacid M. RAS oncogenes: the first 30 years. Nat Rev Cancer 2003;3(6):459–65.
[3] Giehl K. Oncogenic Ras in tumour progression and metastasis. Biol Chem 2005;386(3):193–205.
[4] Aoki Y, Niihori T, Narumi Y, Kure S, Matsubara Y. The RAS/MAPK syndromes: novel roles of the RAS pathway in human genetic disorders. Hum Mutat 2008;29(8):992–1006.

[5] Tidyman WE, Rauen KA. The RASopathies: developmental syndromes of Ras/MAPK pathway dysregulation. Curr Opin Genet Dev 2009;19(3):230–6.
[6] Rauen KA. The RASopathies. Annu Rev Genomics Hum Genet 2013;14:355–69.
[7] Aoki Y, Niihori T, Inoue S, Matsubara Y. Recent advances in RASopathies. J Hum Genet 2016;61(1):33–9.
[8] van der Burgt I. Noonan syndrome. Orphanet J Rare Dis 2007;2:4.
[9] Romano AA, Allanson JE, Dahlgren J, Gelb BD, Hall B, Pierpont ME, et al. Noonan syndrome: clinical features, diagnosis, and management guidelines. Pediatrics 2010;126(4):746–59.
[10] Tartaglia M, Mehler EL, Goldberg R, Zampino G, Brunner HG, Kremer H, et al. Mutations in PTPN11, encoding the protein tyrosine phosphatase SHP-2, cause Noonan syndrome. Nat Genet 2001;29(4):465–8.
[11] Gripp KW, Aldinger KA, Bennett JT, Baker L, Tusi J, Powell-Hamilton N, et al. A novel rasopathy caused by recurrent de novo missense mutations in PPP1CB closely resembles Noonan syndrome with loose anagen hair. Am J Med Genet A 2016;170(9):2237–47.
[12] Tidyman WE, Rauen KA. Pathogenetics of the RASopathies. Hum Mol Genet 2016;25(R2):R123-32.
[13] Aoki Y, Niihori T, Banjo T, Okamoto N, Mizuno S, Kurosawa K, et al. Gain-of-function mutations in RIT1 cause Noonan syndrome, a RAS/MAPK pathway syndrome. Am J Hum Genet 2013;93(1):173–80.
[14] Lee CH, Della NG, Chew CE, Zack DJ. Rin, a neuron-specific and calmodulin-binding small G-protein, and Rit define a novel subfamily of ras proteins. J Neurosci 1996;16(21):6784–94.
[15] Shao H, Kadono-Okuda K, Finlin BS, Andres DA. Biochemical characterization of the Ras-related GTPases Rit and Rin. Arch Biochem Biophys 1999;371(2):207–19.
[16] Hoshino M, Yoshimori T, Nakamura S. Small GTPase proteins Rin and Rit Bind to PAR6 GTP-dependently and regulate cell transformation. J Biol Chem 2005;280(24):22868–74.
[17] Shi GX, Cai W, Andres DA. Rit subfamily small GTPases: regulators in neuronal differentiation and survival. Cell Signal 2013;25(10):2060–8.
[18] Wes PD, Yu M, Montell C. RIC, a calmodulin-binding Ras-like GTPase. EMBO J 1996;15(21):5839–48.
[19] Shi GX, Andres DA. Rit contributes to nerve growth factor-induced neuronal differentiation via activation of B-Raf-extracellular signal-regulated kinase and p38 mitogen-activated protein kinase cascades. Mol Cell Biol 2005;25(2):830–46.
[20] Shi GX, Jin L, Andres DA. A rit GTPase-p38 mitogen-activated protein kinase survival pathway confers resistance to cellular stress. Mol Cell Biol 2011;31(10):1938–48.
[21] Shi GX, Cai W, Andres DA. Rit-mediated stress resistance involves a p38-mitogen- and stress-activated protein kinase 1 (MSK1)-dependent cAMP response element-binding protein (CREB) activation cascade. J Biol Chem 2012;287(47):39859–68.
[22] Cai W, Rudolph JL, Sengoku T, Andres DA. Rit GTPase regulates a p38 MAPK-dependent neuronal survival pathway. Neurosci Lett 2012;531(2):125–30.
[23] Meyer Zum Buschenfelde U, Brandenstein LI, von Elsner L, Flato K, Holling T, Zenker M, et al. RIT1 controls actin dynamics via complex formation with RAC1/CDC42 and PAK1. PLoS Genet 2018;14(5):e1007370.
[24] Cai W, Rudolph JL, Harrison SM, Jin L, Frantz AL, Harrison DA, et al. An evolutionarily conserved Rit GTPase-p38 MAPK signaling pathway mediates oxidative stress resistance. Mol Biol Cell 2011;22(17):3231–41.
[25] Gomez-Segui I, Makishima H, Jerez A, Yoshida K, Przychodzen B, Miyano S, et al. Novel recurrent mutations in the RAS-like GTP-binding gene RIT1 in myeloid malignancies. Leukemia 2013;27(9):1943–6.
[26] Berger AH, Imielinski M, Duke F, Wala J, Kaplan N, Shi GX, et al. Oncogenic RIT1 mutations in lung adenocarcinoma. Oncogene 2014;33(35):4418–23.
[27] Comprehensive molecular profiling of lung adenocarcinoma, Nature 2014;511(7511):543–50.
[28] Xu F, Sun S, Yan S, Guo H, Dai M, Teng Y. Elevated expression of RIT1 correlates with poor prognosis in endometrial cancer. Int J Clin Exp Pathol 2015;8(9):10315–24.
[29] Feng YF, Lei YY, Lu JB, Xi SY, Zhang Y, Huang QT, et al. RIT1 suppresses esophageal squamous cell carcinoma growth and metastasis and predicts good prognosis. Cell Death Dis 2018;9(11):1085.
[30] Yaoita M, Niihori T, Mizuno S, Okamoto N, Hayashi S, Watanabe A, et al. Spectrum of mutations and genotype-phenotype analysis in Noonan syndrome patients with RIT1 mutations. Hum Genet 2016;135(2):209–22.
[31] Roberts AE, Allanson JE, Tartaglia M, Gelb BD. Noonan syndrome. Lancet (London, England) 2013;381(9863):333–42.
[32] Inoue S, Moriya M, Watanabe Y, Miyagawa-Tomita S, Niihori T, Oba D, et al. New BRAF knockin mice provide a pathogenetic mechanism of developmental defects and a therapeutic approach in cardio-facio-cutaneous syndrome. Hum Mol Genet 2014;23(24):6553–66.
[33] Matsumura H, Hasuwa H, Inoue N, Ikawa M, Okabe M. Lineage-specific cell disruption in living mice by Cre-mediated expression of diphtheria toxin A chain. Biochem Biophys Res Commun 2004;321(2):275–9.
[34] Inoue SI, Takahara S, Yoshikawa T, Niihori T, Yanai K, Matsubara Y, et al. Activated Braf induces esophageal dilation and gastric epithelial hyperplasia in mice. Hum Mol Genet 2017;26(23):4715–27.
[35] Moriya M, Inoue S, Miyagawa-Tomita S, Nakashima Y, Oba D, Niihori T, et al. Adult mice expressing a Braf Q241R mutation on an ICR/CD-1 background exhibit a cardio-facio-cutaneous syndrome phenotype. Hum Mol Genet 2015;24(25):7349–60.
[36] Oba D, Inoue SI, Miyagawa-Tomita S, Nakashima Y, Niihori T, Yamaguchi S, et al. Mice with an oncogenic HRAS mutation are resistant to high-fat diet-induced obesity and exhibit impaired hepatic energy homeostasis. EBioMedicine 2018;27:138–50.
[37] Reuther GW, Der CJ. The Ras branch of small GTPases: Ras family members don't fall far from the tree. Curr Opin Cell Biol 2000;12(2):157–65.
[38] Ma J, Karplus M. Molecular switch in signal transduction: reaction paths of the conformational changes in ras p21. Proc Natl Acad Sci U S A 1997;94(22):11905–10.
[39] Hall BE, Bar-Sagi D, Nassar N. The structural basis for the transition from Ras-GTP to Ras-GDP. Proc Natl Acad Sci U S A 2002;99(19):12138–42.
[40] Mir S, Cai W, Carlson SW, Saatman KE, Andres DA. IGF-1 mediated neurogenesis involves a novel RIT1/Akt/Sox2 cascade. Sci Rep 2017;7(1):3283.
[41] Araki T, Mohi MG, Ismat FA, Bronson RT, Williams IR, Kutok JL, et al. Mouse model of Noonan syndrome reveals cell type- and gene dosage-dependent effects of Ptpn11 mutation. Nat Med 2004;10(8):849–57.
[42] Schuhmacher AJ, Guerra C, Sauzeau V, Canamero M, Bustelo XR, Barbacid M. A mouse model for Costello syndrome reveals an Ang II-mediated hypertensive condition. J Clin Invest 2008;118(6):2169–79.
[43] Marin TM, Keith K, Davies B, Conner DA, Guha P, Kalaitzidis D, et al. Rapamycin reverses hypertrophic cardiomyopathy in a mouse model of LEOPARD syndrome-associated PTPN11 mutation. J Clin Invest 2011;121(3):1026–43.
[44] Hernández-Porras I, Fabbiano S, Schuhmacher AJ, Aicher A, Cañamero M, Cámara JA, et al. K-RasV14I recapitulates Noonan syndrome in mice. Proc Natl Acad Sci 2014;111(46):16395–400.
[45] Gabbiani G, Ryan GB, Majne G. Presence of modified fibroblasts in granulation tissue and their possible role in wound contraction. Experientia 1971;27(5):549–50.
[46] Oka T, Xu J, Kaiser RA, Melendez J, Hambleton M, Sargent MA, et al. Genetic manipulation of periostin expression reveals a role in cardiac hypertrophy and ventricular remodeling. Circ Res 2007;101(3):313–21.
[47] Brooks WW, Conrad CH. Isoproterenol-induced myocardial injury and diastolic dysfunction in mice: structural and functional correlates. Comp Med 2009;59(4):339–43.
[48] Hattori T, Murase T, Takatsu M, Nagasawa K, Matsuura N, Watanabe S, et al. Dietary salt restriction improves cardiac and adipose tissue pathology independently of obesity in a rat model of metabolic syndrome. J Am Heart Assoc 2014;3(6):e001312.
[49] Jover B, Reynes C, Rugale C, Reboul C, Jeanson L, Tournier M, et al. Sodium restriction modulates innate immunity and prevents cardiac remodeling in a rat model of metabolic syndrome. Biochim Biophys Acta (BBA) Mol Basis Dis 2017;1863(6):1568–74.
[50] Travers JG, Kamal FA, Robbins J, Yutzey KE, Blaxall BC. Cardiac fibrosis: the fibroblast awakens. Circ Res 2016;118(6):1021–40.
[51] Tian J, An X, Niu L. Myocardial fibrosis in congenital and pediatric heart disease. Exp Ther Med 2017;13(5):1660–4.
[52] Tallquist MD, Molkentin JD. Redefining the identity of cardiac fibroblasts. Nat Rev Cardiol 2017;14(8):484–91.
[53] Hirsch HD, Gelband H, Garcia O, Gottlieb S, Tamer DM. Rapidly progressive obstructive cardiomyopathy in infants with Noonan's syndrome. Report of two cases. Circulation 1975;52(6):1161–5.
[54] Poterucha JT, Johnson JN, O'Leary PW, Connolly HM, Niaz T, Maleszewski JJ, et al. Surgical ventricular septal myectomy for patients with Noonan syndrome and symptomatic left ventricular outflow tract obstruction. Am J Cardiol 2015;116(7):1116–21.
[55] Zhang W, Yano N, Deng M, Mao Q, Shaw SK, Tseng YT. beta-Adrenergic receptor-PI3K signaling crosstalk in mouse heart: elucidation of immediate downstream signaling cascades. PLoS One 2011;6(10):e26581.
[56] Matsui T, Li L, Wu JC, Cook SA, Nagoshi T, Picard MH, et al. Phenotypic spectrum caused by transgenic overexpression of activated Akt in the heart. J Biol Chem 2002;277(25):22896–901.
[57] Shioi T, McMullen JR, Kang PM, Douglas PS, Obata T, Franke TF, et al. Akt/protein kinase B promotes organ growth in transgenic mice. Mol Cell Biol 2002;22(8):2799–809.
[58] Lian H, Ma Y, Feng J, Dong W, Yang Q, Lu D, et al. Heparin-binding EGF-like growth factor induces heart interstitial fibrosis via an Akt/mTor/p70s6k pathway. PLoS One 2012;7(9):e44946.
[59] Landry NM, Cohen S, Dixon IMC. Periostin in cardiovascular disease and development: a tale of two distinct roles. Basic Res Cardiol 2018;113(1):1.
[60] Wang J, Chandrasekhar V, Abbadessa G, Yu Y, Schwartz B, Kontaridis MI. In vivo efficacy of the AKT inhibitor ARQ 092 in Noonan Syndrome with multiple lentigines-associated hypertrophic cardiomyopathy. PLoS One 2017;12(6):e0178905.
[61] Clay SA, Domeier TL, Hanft LM, McDonald KS, Krenz M. Elevated Ca2+ transients and increased myofibrillar power generation cause cardiac hypercontractility in a model of Noonan syndrome with multiple lentigines. Am J Physiol Heart Circ Physiol 2015;308(9):H1086–95.
[62] Hahn A, Lauriol J, Thul J, Behnke-Hall K, Logeswaran T, Schanzer A, et al. Rapidly progressive hypertrophic cardiomyopathy in an infant with Noonan syndrome with multiple lentigines: palliative treatment with a rapamycin analog. Am J Med Genet A 2015;167a(4):744–51.
[63] Araki T, Chan G, Newbigging S, Morikawa L, Bronson RT, Neel BG. Noonan syndrome cardiac defects are caused by PTPN11 acting in endocardium to enhance endocardial-mesenchymal transformation. Proc Natl Acad Sci U S A 2009;106(12):4736–41.
[64] Hernandez-Porras I, Schuhmacher AJ, Garcia-Medina R, Jimenez B, Canamero M, de Martino A, et al. K-Ras(V14I) -induced Noonan syndrome predisposes to tumour development in mice. J Pathol 2016;239(2):206–17.